Journal of Engineering Science and Technology
Special Issue on Development of Sustainability Systems - III, 17 - 34

PRESSURE DROP DETERMINATION AND ANALYSIS IN A CIRCULAR MICROCHANNEL HEAT EXCHANGER

ALI M. MOHSEN[1,*], HUSSAIN H. AL-KAYIEM[2], RAED A. JESSAM[3], IBRAHIM M. MOHAMED[4]

[1]School of Engineering, Faculty of Innovation and Technology, Taylor's University, 47500 Subang Jaya, Malaysia
[2]College of Engineering Technologies, University of Hilla, 51001 Al-Hill, Babylon, Iraq
[3]Electromechanical Engineering Department, University of Technology, Baghdad, Iraq
[4]Mechanical Engineering Department, Universiti Teknologi PETRONAS, 32610 Seri Iskandar, Perak, Malaysia
*Corresponding author: eng.ali2008@yahoo.com

Abstract

Pressure drop in microchannel heat exchangers (MCHEX) represents a challenge to be managed for proper and efficient operation. The objective of the current paper is to experimentally, theoretically, and computationally investigate the pressure drop across an MCHEX and justify the discrepancy in the results achieved by the three estimation methods. The investigated MCHEX comprises 20 micro-tubes of 1 mm diameter and 50 mm long connecting two circular headers of 5 mm diameter. The computational simulations were conducted using ANSYS Fluent 2020R1 at five different flow rates covering a range of Reynolds numbers from 1,500 to 7,500. The experimental setup was developed, comprising a microchannel heat exchanger, peristaltic pump, flow controller, and digital differential pressure manometer. The theoretical evaluation was conducted based on the well-established Darcy-Weisbach and Colebrook correlations. The computational procedure was validated by comparison with the experimental results, achieving a mean percentage of relative error in the velocity of 11.2%. A significant pressure drop discrepancy was observed: for Re = 7,500, the experimental pressure drop reached 30.5 kPa, while CFD and theoretical values were 20.3 and 7.7 kPa, respectively. The significant finding is the large margin of error between the experimental, numerical, and mathematical pressure drop results. These findings confirm that assuming pipe flow behaviour in MCHEX headers leads to major prediction errors.

Keywords: Flow distribution, Maldistribution, Microchannel heat exchanger, Microtube, Pressure drop, Protrusion.

1. Introduction

Microchannel heat exchangers (MCHEXs) are compact, high-efficiency heat exchangers that use multiple parallel micro-scale channels to enhance heat transfer [1]. Their design offers a high surface-area-to-volume ratio, enabling efficient thermal performance with reduced material and refrigerant usage [2]. MCHEXs are increasingly used in HVAC, automotive, and industrial applications due to their lightweight structure and superior thermal efficiency [3] However, the industry is still facing several challenges in designing a performance-wise optimized micro-channel heat exchanger [4, 5]. One of the major problems is the maldistribution of refrigerant flowing from the header into several micro-channels [6]. Kays and London [7] discussed a compact heat exchanger header theory, which specializes in headers with oblique nozzles. This is often the first known source of a standard rule of thumb that the header pressure drop should be approximately 10% or less of the core pressure drop for flow maldistribution to be negligible. The value of 10% is biased as they did not have any quantitative analysis or experimental data to support the claim. The authors concluded that in practice, designing headers with a low-pressure drop is challenging, thus motivating thoughtful header designs.

Single-phase pressure drop inside a microchannel heat exchanger was comprehensively tested by Yin et al. [8]. The experimental data were used to calculate local pressure drop coefficients, which were then compared to published correlations. The results confirmed that the Moody chart was applicable to submillimetre channel flows. In their work, two types of manufacturing defects were quantified using nonintrusive tests followed by destructive evaluation: variation of microchannel port diameters and port blockage by brazing flux. A pressure drop model for the entire microchannel heat exchanger was developed, which predicted the pressure and mass flow rate distribution within the microchannel heat exchanger. The developed model can be used as a design tool to optimize microchannel dimensions and heat exchangers' circuitry. Pressure drop of liquid flow through rectangular cross-section microchannels was investigated experimentally by Akbari et al. [9]. Soft lithography was used to create polydimethylsiloxane microchannels. With distilled water as the working fluid, pressure drop data were used to describe the friction factor with different aspect ratios ranging from 0.13 to 0.76 and Reynolds numbers from 1 to 35. The results were compared to a general model designed to predict the fully developed pressure drop in microchannels with arbitrary cross-sections. The effects of various losses, such as developing area, minor flow contraction and expansion, and streaming potential, were studied using available theories on the measured pressure drop. The experimental results were in close agreement with the theoretical calculations based on pressure drop in arbitrary cross-sectional channels.

Several works have numerically investigated the flow distribution in conventional heat exchangers [10-12]. Some have mainly focused on the headers' configuration on the device performance [13-15]. However, studies focusing specifically on MCHEXs remain limited [16]. Wang et al. [16, 17] performed numerical investigations with complementary experiments observing typical and advanced oblique flow headers for a compact heat exchanger with inside diameters of 2 and 3 mm. In the first study, the micro-tubes were constructed as a simplified 1×9 array. They concluded that having the inlet and outlet nozzles connected to the same side for oblique flow headers will increase flow uniformity. In the second paper, five modified header geometries were investigated to target flow uniformity while achieving negligible pressure drop. It was reported that gravity has an insignificant impact on flow uniformity. However, by measuring the flow inside each channel, the flow distribution was found to be highly dependent on the header design and inlet flow velocity. The flow distribution is significantly improved by lifting the jet stream using the modified header with a baffle tube, followed by the baffle plate and multi-step header. Similar observations were reported by Lance and Carlson [18], as it was found that higher flow rates produced less uniform flow for a traditional nozzle orientation, as the jet directly impacted the channel cortical region.

The thermal efficiency in MCHEXs highly depends on the flow uniformity, i.e., maldistribution and pressure drop [19-21]. Despite the extensive research on microchannel heat exchangers, there remains a significant gap in understanding the connectivity of the risers to the headers on pressure drop and flow uniformity, particularly in MCHEXs [16, 17, 22]. Existing studies have only partially explored this design aspect, often without a comprehensive evaluation of the resulting hydrodynamic effects. The recommendations of previous works to use protrusions are meant for better maldistribution, while the physical reason has not been addressed till the recommendation of Al-Bayati et al. [6] to further investigate the structure of the flow exit from the microchannels into the outlet header in the shape of jet flow. This observation justifies the discrepancy in predicting the pressure drop in microchannels. They recommended further extending the study of circular microchannels by CFD with a focus on the pressure drop in the MCHEX to justify the discrepancy between measurement and prediction results.

Therefore, the present study addresses this gap by combining experimental measurements, numerical simulations, and theoretical analysis to investigate the pressure drop in MCHEXs. This work offers novel insights that can support more effective design strategies for enhancing performance and reliability in microchannel-based thermal systems by modifying the connection configuration of the microtubes to the outlet header.

2. Methodology

The pressure drops across the MCHEX was determined by theoretical, experimental, and numerical methods and compared at various flow rates. This requires the design and fabrication of an experimental setup that permits measurements of the flow variables. Besides, a mathematical procedure has been adopted to predict the pressure drop across the microchannel heat exchanger, which is mainly based on the well-established Darcy-Weisbach equation. The investigation was performed over a range of inlet flow rates of 308, 617, 923, 1234, and 1543 ml/m, which correspond to Re values of 1,500, 3,000, 4,500, 6,000, and 7,500.

2.1. Experimental methodology

The experimental process is discussed and explained briefly, starting from the technical drawings for the two protrusion configuration types, passing through the prototype's desired parameters, and ending with the measurement variables. The manifold considered throughout this work is constant in its cross-sectional area.

2.1.1. Experimental modelling and fabrication

The engineering layout of the experimental prototype of the MCHE is shown in Fig. 1. Note that the terms "micro-channel," inflow port," and "outflow port" are used interchangeably throughout this work. The illustrations are not drawn to scale. The geometrical parameters in the current investigation to design and fabricate the microchannels are basically adopted from the industrial microchannels used by Khan and Fartaj [23]. The values of the geometries are shown in Table 1. The MCHEX uses circular micro-tubes with 1.0 mm diameter and 0.96 mm spacing and inlet/outlet headers with 5 mm diameter.

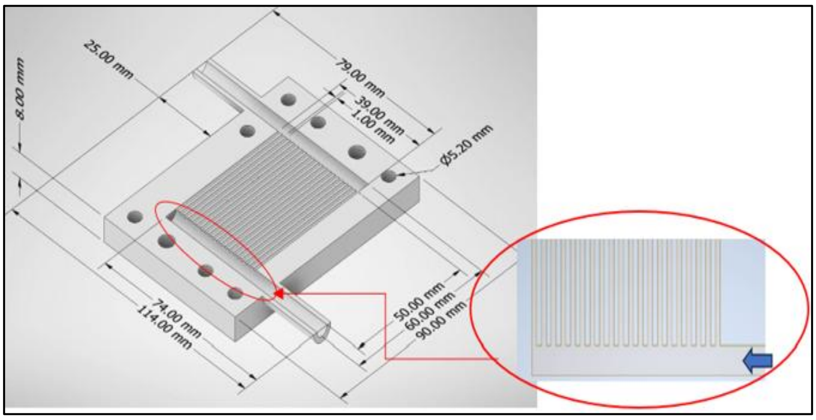

Fig. 1. Configurations and geometries of the prototypes.

Table 1. Details of microchannel heat exchange dimensions.

Parameters	Value
Channel type	Circular channel
Header diameter (Manifold Diameter), Dh	5 mm
Outflow port diameter, D_c	0.96 mm
Channel Spacing, S	0.96 mm
Length of the manifold, L	60 mm
Number of ports, n	20
Length of port (Microchannel length)	50 mm

2.1.2. Experimental setup

The experimental setup is shown schematically in Fig. 2. Water flow is discharged and controlled by a Peristaltic pump through a 6.4-mm-diameter plastic tube connected to the 5-mm-diameter inlet header of the MCHEX. Water flows up in 20 MC risers with 0.96-mm-diameter after the coating process during the fabrication process and exits at the top into the 5-mm-diameter outlet header. A digital differential pressure manometer is connected at the headers' inlet and outlet to measure the pressure drop across the MCHEX.

Figure 3 shows the model after fabrication using the stereolithography 3D printing method with a clear resin, allowing the instrumentation to analyse the model's readings.

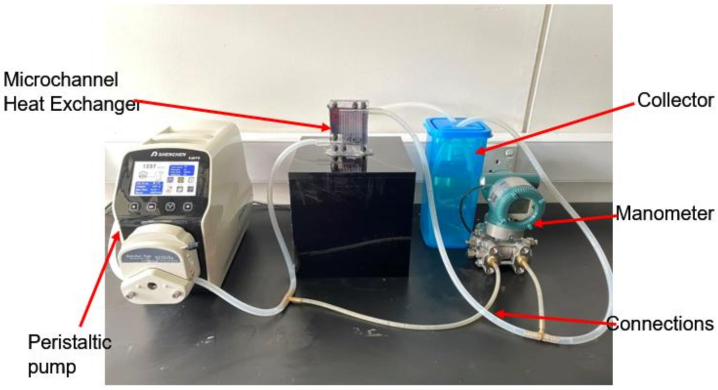

Fig. 2. Schematic of the experimental setup.

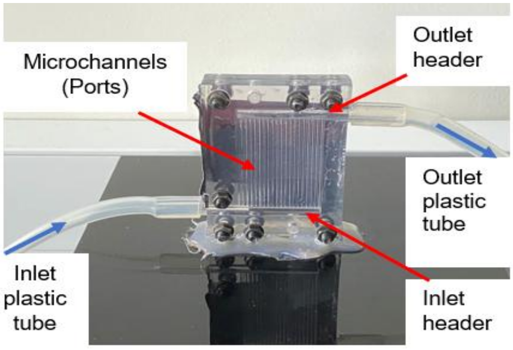

Fig. 3. 3D printed microchannel heat exchanger.

The pressure difference across the microchannel heat exchanger was measured experimentally between the inlet and outlet flow in the plastic tubes using a differential pressure micromanometer. Five different flow rates with five different corresponding Reynolds numbers ranging from 1,500 to 7,500 based on the header diameter have been considered.

2.2. Computational methodology

In their experimental and numerical investigations, Liu and Garimella [24] have demonstrated that the flow analysis of MCHEX by commercial software packages is satisfactory and can be employed to aid the study of flow characteristics in MCs. Accordingly, to reduce the time and cost of a wide range of Re, ANSYS Fluent 2020 R1 commercial software has been adopted in the current investigations to extend the two values of experimental Re to five values of numerical Re.

2.2.1. Computational model and boundary conditions

The computational fluid dynamics (CFD) software ANSYS Fluent 2020 R1 was used to solve the three-dimensional fluid flow equations. The fluid flow in the MCHEX was assumed to be steady-state and incompressible. The simulation was performed with the help of a pressure-based solver. The working fluid is a single-phase water-liquid at room temperature of 25 ºC with a density of 997 kg/m3 and viscosity of 0.89 mPa.s. Water flows from the lower inlet header in Fig. 4, passing through the microtubes to the upper outlet header. The gravity effects on flow are negligible. The geometry was extracted using a volume extractor, as shown in Fig. 4, using space claim on ANSYS Fluent 2020 R1 with the exact volume dimensions of the actual prototype used in the experiment. No wall thickness was added in the numerical simulations since this study focuses mainly on the pressure drop within the micro-channel heat exchanger and not on the walls' heat transfer.

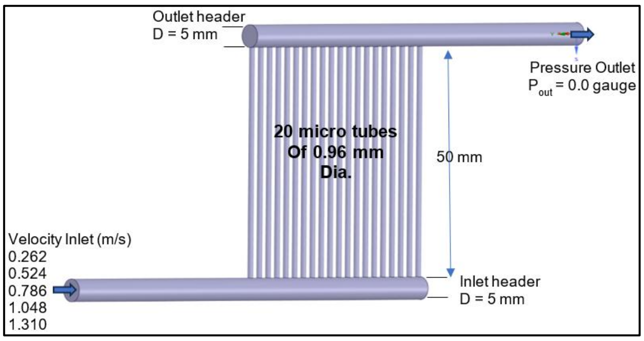

Fig. 2. Computational model of the MCHE and the simulation boundary conditions in ANSYS-FLUENT.

2.2.2. Meshing criteria and mesh independency check

The meshing process of the MCHE was carried out in two phases: meshing the inlet and outlet headers and meshing the microtube ports. Different mesh sizes were applied to each section of the device. The mesh used in the setup has a total number of elements of 11.432 million with an excellent average aspect ratio of 1.8488 < 5 and an average orthogonal quality of 0.77188.

A grid independence test was performed to ensure high accuracy with less computational time. Four different mesh levels of 4.909 million, 6.325 million, 8.378 million, and 11.432 million cells were tested at a Re of 1,500. The relative error in the average velocity at a fixed point inside the MCHEX for all cases was calculated based on Equation 1 and listed in Table 2. It can be concluded that the computational model with 11.432 million provided a reasonable error for the average velocity value at a fixed point inside the MCHE compared to the other models with a different number of elements.

$$e_n\,\% = \left| \frac{V_n - V_{(n-1)}}{V_n} \right| \times 100 \tag{1}$$

Table 2. Mesh independency test.

No.	Re	Number of elements	Velocity (m/s)	Difference (%)
1	1500	4,909,915	0.2435	-
2	1500	6,325,274	0.2450	0.61
3	1500	8,378,822	0.2449	0.57
4	1500	11,432,581	0.2447	0.49

2.2.3. Governing equations

The governing equations of incompressible flow in the MCHE are provided below, Munson et al. [25], Hasan and Tbena [26], Hasan et al. [27] and Bayrak et al. [28] in detail: Continuity and momentum Eqs. (2), (3) to (4) and (5), for steady-state and 3D fluid flow used can be expressed respectively:

$$\frac{\partial(\rho v_x)}{\partial x}+\frac{\partial(\rho v_y)}{\partial y}+\frac{\partial(\rho v_z)}{\partial z}=0 \tag{2}$$

$$\rho\left(v_x\frac{\partial v_x}{\partial x}+v_y\frac{\partial v_x}{\partial y}+v_z\frac{\partial v_x}{\partial z}\right)=-\frac{\partial P}{\partial x}+\mu\left(\frac{\partial^2 v_x}{\partial x^2}+\frac{\partial^2 v_x}{\partial y^2}+\frac{\partial^2 v_x}{\partial z^2}\right) \tag{3}$$

$$\rho\left(v_x\frac{\partial v_y}{\partial x}+v_y\frac{\partial v_y}{\partial y}+v_z\frac{\partial v_y}{\partial z}\right)=-\frac{\partial P}{\partial y}+\mu\left(\frac{\partial^2 v_y}{\partial x^2}+\frac{\partial^2 v_y}{\partial y^2}+\frac{\partial^2 v_y}{\partial z^2}\right) \tag{4}$$

$$\rho\left(v_x\frac{\partial v_z}{\partial x}+v_y\frac{\partial v_z}{\partial y}+v_z\frac{\partial v_z}{\partial z}\right)=-\frac{\partial P}{\partial z}+\mu\left(\frac{\partial^2 v_z}{\partial x^2}+\frac{\partial^2 v_z}{\partial y^2}+\frac{\partial^2 v_z}{\partial z^2}\right)+\rho g_z \tag{5}$$

The realizable *k-ε* model with scalable wall function and default settings of the model constants was chosen to solve the continuous flow [29]. The realizable *k-ε* is based on modified transport equations for an alternative formulation for the turbulent kinetic energy, *k,* and its dissipation rate, *ε*. Flow transforms from laminar characteristics to turbulent characteristics.

The transport equations for *k* and ε, in the realizable *k- ε* model Arie et al. [30], are represented below in Eqs. (6) and (7), respectively.

$$\frac{\partial y}{\partial x_j}\left(\rho k u_j\right)=\frac{\partial}{\partial x_j}\left[(\mu+\frac{\mu_t}{\sigma_k})\frac{\partial k}{\partial x_j}\right]+G_k+G_b+\rho_\varepsilon+Y_M+S_k \tag{6}$$

$$\frac{\partial}{\partial x_j}\left(\rho\varepsilon u_j\right)=\frac{\partial}{\partial x_j}\left[(\mu+\frac{\mu_t}{\sigma_\varepsilon})\frac{\partial \varepsilon}{\partial x_j}\right]+\rho C_1 S_\varepsilon+\rho C_2\frac{\varepsilon^2}{k+\sqrt{v_\varepsilon}}+C_{1\varepsilon}\frac{\varepsilon}{k}C_{3\varepsilon}G_b+S_\varepsilon \tag{7}$$

where,

$$C_1=max\left[0.43\frac{\eta}{\eta+5}\right]$$

$$\eta=\ S\frac{k}{\varepsilon}$$

$$S=\ \sqrt{2S_{ij}S_{ij}}$$

In these equations, G_k characterizes the production of turbulence kinetic energy due to the mean velocity gradients, and G_b is the initiation of turbulence kinetic energy due to the buoyancy effect. Y_M represents the involvement of the fluctuating turbulence in the overall dissipation rate; C_1 and $C_{1\varepsilon}$ are constants. σ_k and σ_ε are the turbulent Prandtl numbers for *k* and *ε*, respectively. S_k and S_ε are the user-defined source terms. The model constants have been determined to guarantee that the model operates well for specific undisputed flows, Hanjalic and Launder [31]. The function of Prandtl numbers σ_k and σ_ε is to connect the diffusivities of *k* and *ε* to the eddy viscosity, μ_t. So that its effect is accounted for within the gradient diffusion term of the turbulent transport equations, Versteeg and Malalasekera [32]. The expansion parameter, *η* defined as the ratio of the turbulence to the mean-strain time scales. And S_{ij} is the strain-rate tensor, which is calculated indirectly by using the gradient transport hypothesis presented in Shih et al. [33]. Therefore, the following constants have been established by a comprehensive data fitting for the realizable *k-ε* model [25] such as $C_{1\varepsilon}=1.44, C_2=1.92, \sigma_k=1.0, \sigma_\varepsilon=1.2$.

2.2.4. Validation of the computational procedure

Proper validation of the computational procedure is a vital issue as the main justification for the high discrepancy in the pressure drop based on the visualization of the flow created by the CFD simulation. The numerical results were validated by comparison of the numerically predicted velocities in the microtube with the experimentally measured velocities using the PIV technique. The comparison results are shown in Fig. 5. Three microchannels, namely, MC-01, MC-10, and MC-20, have been selected to cover the entire range of the microtubes risers' system at Re of 1,500 and 3,000. In all of the compared cases, the numerical prediction was higher than the measured velocities. The maximum relative percentage of error between the computational and experimental results is 9.0%, which indicates acceptable agreement, as the simulated flow field is complex and contains a large number of flow disturbances.

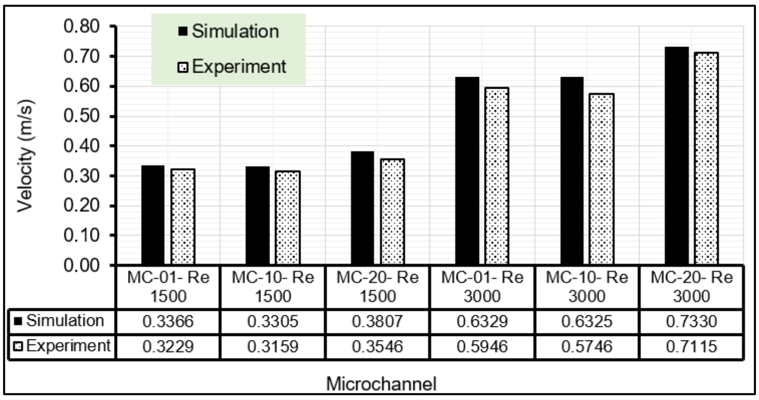

Fig. 5. Validation of the numerical procedure by comparison of the velocity results as predicted by the simulation and measured experimentally.

Furthermore, another validation has been performed to include the entire number of microtubes. Table 3 shows a comparison of the simulation and experimental results of the velocities in the microtubes for the flow rate of 308 ml/min, which corresponds to a Re of 1,500. The results show that the relative percentage of error is acceptable, as the highest is 6.74%, and the mean of all microtubes is 3.86%.

Table 3. Validation by comparison of the computational and experimental velocities in the microtubes at Re = 1,500.

Microtube	Velocities		Error
	Simulation	Exp.	%
Mc 02	0.340	0.322	5.17
Mc 04	0.339	0.325	4.03
Mc 06	0.350	0.345	1.47
Mc 08	0.362	0.352	2.75
Mc 10	0.330	0.316	4.38
Mc 12	0.360	0.345	4.17
Mc 14	0.353	0.342	3.14
Mc 16	0.373	0.363	2.57
Mc 18	0.389	0.373	4.16

Mc 20	0.381	0.355	6.74
Average	-	-	3.86

2.3. Mathematical methodology

The pressure drops across any fluid flow system is built up by minor losses and frictional losses. In the case of the current MCHEX, there are nine different identified frictional and minor losses, including friction losses in the plastic tube from the measuring point to the inlet to the header, Δptube, inlet, contraction minor losses at header inlet, Δpheader inlet nozzle con., frictional losses in the header up to the inlet to the microtube, Δfriction. Inlet header, losses due to contraction from header to the microtube, Δpchannel con, frictional losses in the microtubes, Δpfriction.channel, minor losses at the micro tube connection to the header, Δpchannel, exit, micro tube exit, Δpfriction out, header frictional losses at the upper header from micro tube exit to the connection point to the plastic tube at the outlet, Δpheader outlet nozzle exp, expansion from header to the plastic tube, and finally the frictional losses in the plastic tube, Δptube, out. The total pressure losses across the MCHEX, Δptotal, is the sum of all of them [8, 34-36]. The spots of minor and frictional losses are explained and shown in Fig. 6.

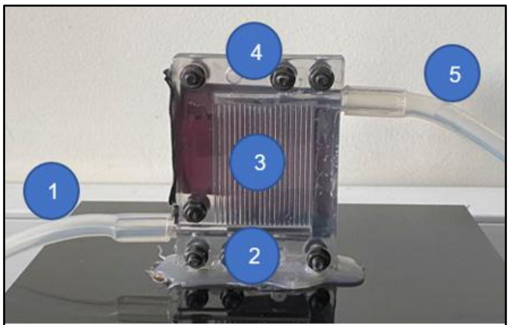

1: The inlet tube losses
1-2: Inlet nozzle to Inlet header (Contraction) (Minor lose),
2: Inlet header (Fictional lose),
2-3: Inlet header to ports (Contraction) (Minor lose),
3: Ports friction factor (Fictional lose),
3-4: Ports to Outlet header (Expansion) (Minor lose),
4: Outlet header (Fictional lose),
4-5: Outlet header to Outlet nozzle (Expansion) (Minor lose), and
5: Outlet tube fiction factor (Fictional lose).

Fig. 6. Locations of the frictional and minor losses.

The frictional losses in any flow passage could be predicted by the Darcy-Weisbach equation as Eq. (8).

$$\Delta p = f_D \frac{L}{D_h} \frac{\rho V_{ave}^2}{2}, \quad (8)$$

where Δp is the pressure loss across the heat exchanger system, f_D is the Darcy friction factor, while D and L are the hydraulic diameter and the length of the respective passage. However, V_{ave} and ρ are the average fluid velocity in m/s and the fluid density in kg/m^3, respectively.

Darcy friction factor is obtained from the Moody chart, which depends on the characterization of the fluid, and pipe diameter represents the header's diameter and the velocity of the fluid flow inside the headers of the microchannel heat exchanger. Although in this work, five different flow rates cover a range of Reynolds numbers from 1,500 to 7,500 based on the header diameter, which covers a flow regime of laminar and turbulent, the flow regime was always laminar inside the microchannel ports. The following Eqs. (9) and (10) would express the Darcy friction factor's fluid regime types either at headers or inside the micro tubes.

For Re < 2,200:

$$f_D = \frac{64}{Re} \tag{9}$$

For 2,200 < Re < 10^5:

$$f_D = \frac{0.3164}{Re^{0.25}} \tag{10}$$

All the local pressure drops in piping system fittings could be predicted from the well-established formula of Eq. (11), where,

$$\Delta P = k_{loss} \frac{\rho V_{ave}^2}{2} \tag{11}$$

The average velocity, $V_{ave} = Q/A$. The loss parameter, k_{loss}, could be found in many fluid mechanics books, pressure loss flow charts, and standards.

3. Result and Discussion

The graphical presentations and comparisons of results are mostly formatted in terms of pressure drop variation versus Re values. The simulation results are mostly presented as contours to allow flow visualization inside the MCHEX. The results section first displays the graphical tabulation of the quantitative pressure drop results. Analysis and justification of the high discrepancy are achieved by the CFD flow visualization, which allows insight into monitoring and exploring the flow structures inside the various parts of the MCHEX.

Table 4 presents the numerically predicted pressure drop, the experimentally recorded pressure drop, and the relative percentage of errors between the two values. The table shows that the numerical pressure drops increases from 2.1 kPa to 20.3 kPa as Reynolds's number increases from 1,500 to 7,500. Accordingly, the relative percentage of errors between the experimental measurements and numerical data increases from 4.5% to 33.4% as presented in Table 4. The relative percentage error is shown to be greater for higher Reynolds' number values.

Table 4. Computational and experimental measurement of pressure drop results with the relative percentage of differences.

Reynolds Number	ΔP Bare case (kPa)		Relative
	Experiment	Numerical	error (%)
1,500	2.2	2.1	4.5
3,000	6.2	5.5	11.2
4,500	11.5	9.8	14.7
6,000	20	14.2	29
7,500	30.5	20.3	33.4

3.1. Pressure drop estimation and comparison

To highlight the difference between the experimental measurements, the computational simulations, and the theoretically predicted results, all data are gathered in Fig. 7. At a lower Reynolds number of 1,500, the experimental and numerical pressure drop is found to be 2.2 kPa and 2.1 kPa, respectively. However, a significantly smaller value of 0.7 kPa was obtained from the theoretical calculations. This large margin of error increases for a higher flow Reynolds' number of 7,500 as the pressure drop values of the experimental, numerical, and theoretical results change to 30.5 kPa, 20.3 kPa, and 7.7 kPa, respectively. A similar trend of high difference and increment as Re increased is reported in the experimental measurement by Yin et al. [8]. They suggested that the presence of brazes and a non-correctly predicted loss coefficient were due to non-uniform circular cross-sections.

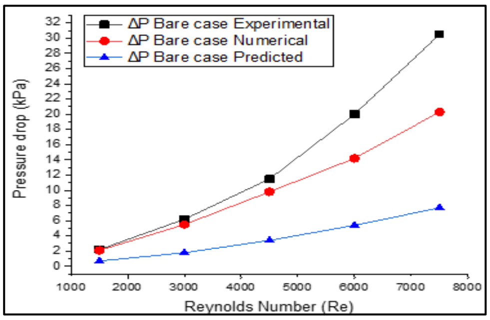

Fig. 7. Experimental, numerical, and predicted pressure drop (ΔP).

The general trend of the pressure drop results is summarized in Fig. 8. The margin of discrepancy is large, and the well-established prediction correlations have failed to estimate the pressure drop in the MCHEX.

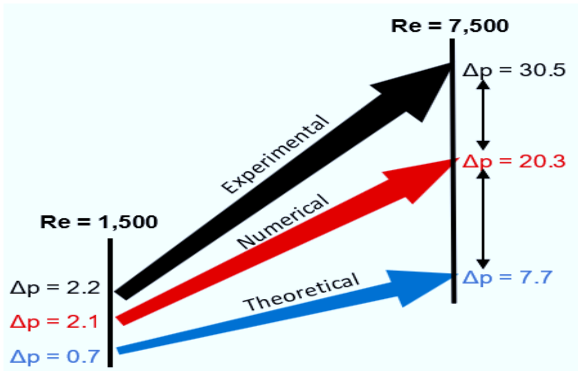

Fig. 8. The general trend, with quantitative values of the pressure drop in the MCHEX.

Now, the objective of the current investigation is to address the reason for the high discrepancy between the experimental, numerical, and theoretical methods to estimate the pressure drop, which is deliberated in the next section.

3.2. Addressing the root cause of the discrepancies

The CFD has a superior feature that allows the flow structure in any flow field to be visualized. The velocity contours produced from CFD simulations of any internal or external flow assist in describing the flow structure and provide reasonable justification for any strange behaviour of the flow or the results.

Figure 9 displays the velocity contours in the MCHEX. The velocity contours are considered to provide a better visualization of the flow structure. The figure on the left side represents the entire MCHEX. The two sub-figures on the right are the enlarged portions of the headers and the connection with the microtubes. The upper right sub-figure is the outlet header, and the lower right sub-figure is the inlet header. The flow exits from the microtube risers, creating a jet-like flow in the outlet header.

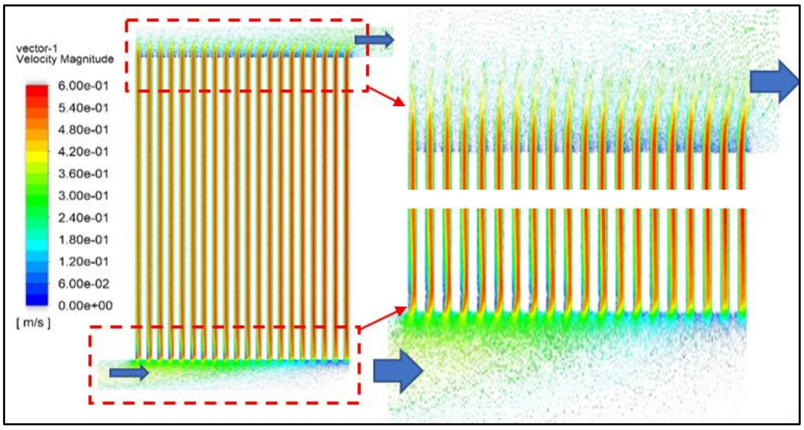

Fig. 9. The velocity contours in the MCHEX, with sub-figures, highlight the flow structure in the inlet and outlet headers.

To further understand the flow structure and its contribution to the high-pressure drop discrepancy, Figures 10 and 11, with Re of 1,500 and 7,500, respectively, have been produced to visualize the inflow from the microtubes into the outlet header. Enlarged velocity vector contours at the outlet portions of MC 1 to 4 and MC 17 to 20 are presented in Fig. 10. The upper part of the figure shows an enlarged view of the outlet of channels 1, 2, 3, and 4. All MCs are experiencing flow with laminar velocity profiles. The mean velocity in MC 1 is around 0.35 m/s, while increasing in the downstream MCs, with a maximum mean velocity of 0.5 m/s in MC 20. The flow is discharging from the MCs' outlets in the form of jet flow and merges with the mainstream in the outlet header. The jet flow is vertical in MCs 1 and 2 and starts to bend slightly in channels 3 and 4. However, looking at the jet flow of the last four MCs, it is clear that the jet angle is high compared to the upstream MCs' jet angle.

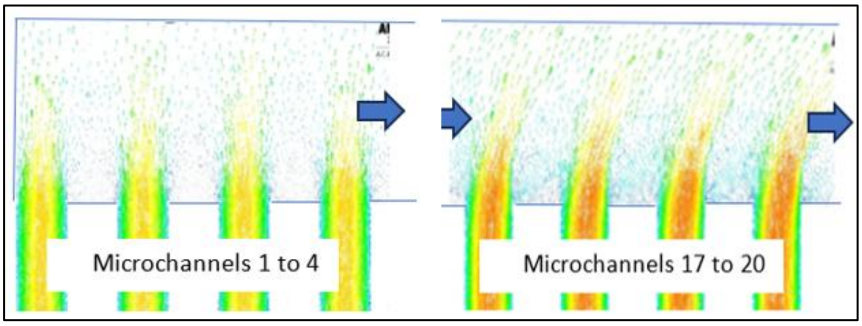

Fig. 10. Enlarged velocity vector field at the outlets of microchannels 1 to 4 and 17 to 20 shows the outlet water jet orientations trend. (Re = 1,500).

An enlarged view of the velocity vector field at the outlets of MCs 1 to 4 and MCs 17 to 20 is presented in Fig. 11 with Re = 7,500. Similar to the case of Re = 1500, jet flow at each outlet from the MCs is destroying the flow uniformity, and there is no stable velocity profile along the outlet header. The jet in the case Re = 7500 is penetrating deeper in the header flow field than the case of Re = 1500. However, in both Re, the laminar velocity profile is attained in all of the channels. This confirms the conclusion of Liu and Garimella [24] that turbulent flow is less likely to happen in MCs with a diameter less than 1 mm.

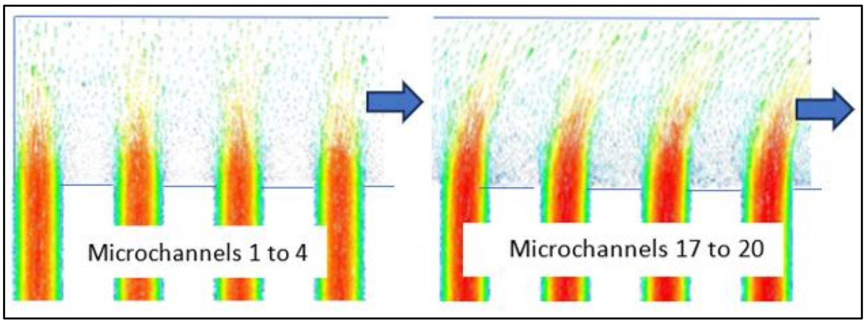

Fig. 11. Enlarged velocity vector field at the outlets of microchannels 1 to 4 and 17 to 20 shows the outlet water jet orientations trend. (Re = 7,500).

Figures 12 and 13 show the pressure profiles for flow rates with 1,500 and 7,500 Re, respectively. The pressure increase was the main reason for increasing the velocity profile, which leads to a maldistribution phenomenon, especially at the pressure profile of Re = 7,500 in the last channels near the outlet port. In the case of Re = 1,500, the inlet's mean pressure is around 2,200 Pa, reduced to 90.4 Pa at the outlet. In the case of Re = 7,500, the mean pressure is around 21,019 Pa, reduced to 779 Pa at the outlet.

These discrepancies confirm that standard pipe flow assumptions are not valid for MCHEX headers and that CFD visualization reveals non-uniform jet structures and maldistribution.

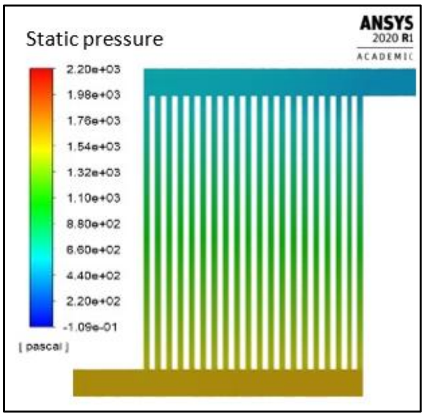

Fig. 12. Static pressure contours for Re 1,500 in the flow field of the MCHE.

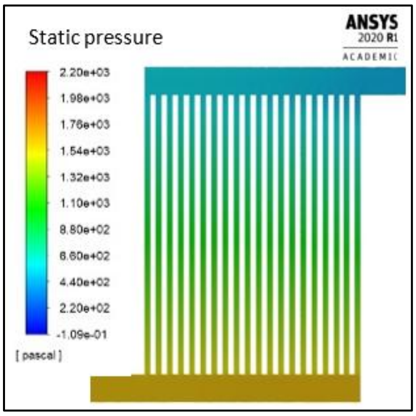

Fig. 13. Static pressure contours for Re 7,500 in the flow field of the MCHE.

4. Conclusions

Pressure drop in the microchannel heat exchanger is measured, simulated, calculated, and compared. A large discrepancy has been realized in the results, mainly in the very low estimation using the well-known correlations in the literature. ANSYS Fluent 2020 R1 was used to simulate the flow field and produce pressure and velocity contours inside the MCHEX at the five different flow rates, referring to Reynolds numbers of 1,500, 3,000, 4,500, 6,000, and 7,500. The numerical procedure is validated by comparing the experimental results with a mean percentage of relative error of 11.2%. These analyses demonstrate that the typical friction factor correlations and local pressure drop coefficients could not be used to predict both the frictional and minor losses in MCHEX. Particular conclusions may be summarized as follows:

- The experimental pressure drop was consistently higher than both numerical and theoretical predictions.
- At Re = 7,500, the theoretical model underestimated the pressure drop by 74.8% compared to experimental results.
- The CFD model underpredicted pressure drops by up to 33.4% at high flow rates.

The pressure drop indicates a significant difference between experimental-numerical and predicted results. The CFD simulations provided helpful aid to justify the high discrepancy, where the flow could not be treated as pipe flow. The flow at the exit of the micro tubes in the outlet header creates jet-like phenomena, which bring the situation away from normal pipe flow. Future work will explore different header geometries, angled risers, and heat transfer performance under two-phase flow conditions.

Acknowledgment

The authors would like to acknowledge Yayasan Universiti Teknologi PETRONAS (YUTP - FRG) for funding the research under CS: 015LC0-026.

Nomenclature

Symbols

C_1	Variable
C_2, $C_{1\varepsilon}$	Constants
$C_{3\varepsilon}$	Buoyancy effect on the dissipation rate
D_h	Header diameter, mm
D_c	Outflow port diameter, mm
f_D	Darcy friction factor
G_k, G_b	Turbulence kinetic energy generation terms
j	Species
k	Turbulence kinetic energy, m^2/s^2
L	Length of the manifold, mm
Q	Volumetric flow rate, m^3/s
S	Modulus of the strain tensor
S_m, S_h, S_k, S_ε	Source terms
V	Velocity, m/s
Y_M	Contribution to the overall dissipation rate

Greek letters

ε	Kinetic energy dissipation rate, m^2/s^3
η	Thermal performance factor
μ	Viscosity, $N.s/m^2$
μ_t	Turbulent viscosity, $N.s/m^2$
ν	Kinematic viscosity, m^2/s
ρ	Density, kg/m^3
σ_k, σ_ε	Turbulent Prandtl numbers

Abbreviations

CFD	Computational Fluid Dynamics
MCHEX	Microchannel Heat Exchanger
Mc	Microtube or microchannel
Re	Reynolds number

References

1. Kashani, A.; Rasheed, R.H.; Hussein, M.A.; Akbari, O.A.; Abdul-Redha, H.K.; Ahmadi, G.; Salahshour, S.; and Sabetvand, R. (2024). Simulation of flow dynamics and heat transfer behavior of nanofluid in a microchannel with rough surfaces. *International Journal of Thermofluids*, 24, 100901.
2. Ali, A.A.; Alfarge, D.; Lafta, A.M.; Hasan, M.I.; and Rashid, F.L. (2024). Numerical investigation for the effects of surface roughness in counter flow microchannel heat exchanger with different channel geometries. *Discover Applied Sciences*, 6(9), 459.
3. Pontes, P.D.; Chenche, L.E.P.; Lima, J.A.; Naveira-Cotta, C.P.; and Moita, A.S. (2025). Optimization of rectangular micro-channel heat exchangers for

use in HCPV panels through a genetic algorithm. *Case Studies in Thermal Engineering*, 70, 106107.

4. Mokrane, M. (2021). Performance analysis of a micro heat exchanger in electronic cooling applications. *Journal of Thermal Engineering*, 7(4), 773-790.
5. Bayat, M. et al. (2024). Entropy and energy analysis of water/silver nanofluid flow in a microchannel by changing the angle of attack of a cam-shaped vortex generator. *International Journal of Thermofluids*, 23, 100719.
6. Al-Bayati, A.D.J.; Abdulwahhab, H.A.; Al-Kayiem, H.H.; and Mohamed, I.M. (2023). Experimental and numerical investigation of flow maldistribution in a circular microchannel heat exchanger at various flow rates. *Journal of Engineering Science and Technology*, 18, 275-287.
7. Kays, W.M.; and London, A.L. (1984). *Compact heat exchangers* (3rd edition). McGraw-Hill Book Company, Inc.
8. Yin, J.M.; Bullard, C.W.; and Hrnjak, P.S. (2002). Single-phase pressure drop measurements in a microchannel heat exchanger. *Heat Transfer Engineering*, 23(4), 3-12.
9. Akbari, M.; Sinton, D.; and Bahrami, M. (2009). Pressure drop in rectangular microchannels as compared with theory based on an arbitrary cross-section. *Journal of Fluids Engineering*, 131(4), 041202.
10. Wei, W.; Ding, E.; and Du, Y. (2024). Performance of dual-row condenser using microplate and conventional folded multiport extruded tube: A prospective pilot study. *Case Studies in Thermal Engineering*, 60, 104663.
11. Karouei, S.H.H.; Abbas, W.N.; Ali, M.; Nayyef, D.R.; Hussein, K.K.A.; Hammoodi, K.A.; and Azizi, S.S.H. (2025). Numerical investigation of the effects of geometric and fluid parameters on the thermal performance of a double-tube spiral heat exchanger with a conical turbulator. *Case Studies in Thermal Engineering*, 65, 105613.
12. Rahman, M.M.; and Bénard, A. (2024). Flow behaviour and design implications of tapered header plate heat exchangers for enhanced performance. *Proceedings of the 9th Thermal and Fluids Engineering Conference* (*TFEC*), Corvallis, United States.
13. Rahman, M.M.; Jakkala, S.G.; and Bénard, A. (2023). Influence of header configuration on flow distribution within a U-type plate heat exchanger. *Proceedings of the 8th Thermal and Fluids Engineering Conference* (*TFEC*), College Park, United States, 1-10.
14. Smetanin, T.R.; Pakholkov, V.V.; Rogozhkin, S.A.; and Shepelev, S.F. (2024). Numerical simulation of fluid dynamics and mixing in headers of sodium-air heat exchangers. *Nuclear Energy and Technology*, 10(1), 27-32.
15. Sohn, S.; Kim, J.S.; and Song, C.H. (2025). A study on the design of the header of a fin-tube heat exchanger in high temperature heat pump. *Journal of Mechanical Science and Technology*, 39(1), 303-313.
16. Wang, C.-C.; Yang, K.-S.; Tsai, J.-S.; and Chen, I.Y. (2011). Characteristics of flow distribution in compact parallel flow heat exchangers, part I: typical inlet header. *Applied Thermal Engineering*, 31(16), 3226-3234.
17. Wang, C.-C.; Yang, K.-S.; Tsai, J.-S.; and Chen, I.Y. (2011). Characteristics of flow distribution in compact parallel flow heat exchangers, part II: modified inlet header. *Applied Thermal Engineering*, 31(16), 3235-3242.

18. Lance, B.W.; and Carlson, M.D. (2017). Printed circuit heat exchanger flow distribution measurements. *Proceedings of the ASME Turbo Expo 2017: Turbomachinery Technical Conference and Exposition*, Charlotte, United States, 50961, V009T38A021.
19. Ferhi, M.; Abidi, S.; Djebali, R.; and Mebarek-Oudina, F. (2024). Assessment of micro-scale heat exchangers' efficiency using the lattice Boltzmann method and design of experiments. *Energy and Built Environment*, 5(6), 840-852.
20. Gradl, P.; Cervone, A.; and Colonna, P. (2025). Enhancement of friction factors for microchannels fabricated using laser powder directed energy deposition. *Materials and Design*, 251, 113673.
21. Tychanicz-Kwiecień, M.; and Gil, P. (2024). Experimental investigation of thermal and flow characteristics of a prototype minichannel heat exchanger. *International Journal of Heat and Mass Transfer*, 231, 125825.
22. Settati, M.; Oliet, C.; Sanmarti, O.; and Oliva, A. (2024). Experimental and numerical pressure drop investigation of a protruding tube microchannel heat exchanger. *Proceedings of the 9th European Thermal Sciences Conference* (*EUROTHERM*), Bled, Slovenia, 2766(1), 012071.
23. Khan, M.G.; and Fartaj, A. (2011). A review on microchannel heat exchangers and potential applications. *International Journal of Energy Research*, 35(7), 553-582.
24. Liu, D.; and Garimella, S.V. (2004). Investigation of liquid flow in microchannels. *Journal of Thermophysics and Heat Transfer*, 18(1), 65-72.
25. Munson, B.R.; Okiishi, T.H.; Huebsch, W.W.; and Rothmayer, A.P. (2013). *Fundamentals of fluid mechanics* (7th edition). John Wiley & Sons.
26. Hasan, M.I.; and Tbena, H.L. (2018). Numerical investigation of microchannel heat sink with MEPCM suspension with different types of PCM. *Al-Qadisiyah Journal for Engineering Sciences*, 11(1), 115-133.
27. Hasan, M.I.; Rageb, A.A.; Yaghoubi, M.; and Homayoni, H. (2009). Influence of channel geometry on the performance of a counter-flow microchannel heat exchanger. *International Journal of Thermal Sciences*, 48(8), 1607-1618.
28. Bayrak, E.; Olcay, A.B.; and Serincan, M.F. (2019). Numerical investigation of the effects of the geometric structure of microchannel heat sink on flow characteristics and heat transfer performance. *International Journal of Thermal Sciences*, 135, 589-600.
29. ANSYS, Inc. (2020). ANSYS Fluent User's Guide, Release 2020 R1. Retrieved October 5, 2025, from https://www.ansys.com
30. Arie, M.A.; Shooshtari, A.H.; Dessiatoun, S.V.; Al-Hajri, E.; and Ohadi, M.M. (2015). Numerical modelling and thermal optimization of a single-phase flow manifold-microchannel plate heat exchanger. *International Journal of Heat and Mass Transfer*, 81, 478-489.
31. Hanjalic, K.; and Launder, B. (2009). *Modelling turbulence in engineering and the environment: second moment routes to closure*. Cambridge University Press, UK.
32. Versteeg, H.K.; and Malalasekera, W. (2007). *An introduction to computational fluid dynamics: the finite volume method*. Pearson Education.

33. Shih, T.-H.; Liou, W.W.; Shabbir, A.; Yang, Z.; and Zhu, J. (1995). A new k-ε eddy viscosity model for high Reynolds number turbulent flows. *Computers & Fluids*, 24(3), 227-238.
34. Chai, L.; Xia, G.; Zhou, M.; and Li, J. (2011). Numerical simulation of fluid flow and heat transfer in a microchannel heat sink with offset fan-shaped reentrant cavities in the sidewall. *International Communications in Heat and Mass Transfer*, 38(5), 577-584.
35. Zhang, X.; Zhao, T.; Wu, S.; and Yao, F. (2019). Experimental study on liquid flow and heat transfer in rough microchannels. *Advances in Condensed Matter Physics*, 2019(1), 1974952.
36. Lance, B.W.; and Carlson, M.D. (2018). Microchannel heat exchanger flow validation study. *Proceedings of the ASME Turbo Expo 2018: Turbomachinery Technical Conference and Exposition*, Oslo, Norway, 51180, V009T38A027.